

# A Markov chain Monte Carlo approach for measurement of jet precession in radio-loud active galactic nuclei

Maya A. Horton,<sup>1</sup>★ Martin J. Hardcastle<sup>1</sup>,<sup>1</sup> Shaun C. Read<sup>2</sup><sup>1</sup>  
and Martin G. H. Krause<sup>1</sup>

<sup>1</sup>Centre for Astrophysics Research, School of Physics, Astronomy and Mathematics, University of Hertfordshire, College Lane, Hatfield AL10 9AB, UK

<sup>2</sup>INAF – Osservatorio Astronomico di Roma, via Frascati 33, I-00040 Monte Porzio Catone, Roma, Italy

Accepted 2020 February 10. Received 2020 February 10; in original form 2019 November 13

## ABSTRACT

Jet precession can reveal the presence of binary systems of supermassive black holes. The ability to accurately measure the parameters of jet precession from radio-loud active galactic nuclei is important for constraining the binary supermassive black hole population, which is expected as a result of hierarchical galaxy evolution. The age, morphology, and orientation along the line of sight of a given source often result in uncertainties regarding the jet path. This paper presents a new approach for efficient determination of precession parameters using a two-dimensional Markov chain Monte Carlo curve-fitting algorithm that provides us a full posterior probability distribution on the fitted parameters. Applying the method to Cygnus A, we find evidence for previous suggestions that the source is precessing. Interpreting in the context of binary black holes leads to a constraint of parsec scale and likely sub-parsec orbital separation for the putative supermassive binary.

**Key words:** methods: data analysis – methods: statistical – galaxies: active – galaxies: jets – radio continuum: galaxies.

## 1 INTRODUCTION

The detection of gravitational waves from black hole mergers has brought new opportunities for exploring the coalescence of binary systems (Abbott et al. 2016a,b, 2017). However, current instrumentation is limited to the detection of stellar-mass black hole mergers. Given that mergers between galaxies are common and play a fundamental role in galactic evolution (e.g. Carpineti et al. 2015; Rodriguez-Gomez et al. 2015), the case has been made that many galaxies may contain binary supermassive black holes (Begelman, Blandford & Rees 1980; Mayer 2017; Tremmel et al. 2018).

If a binary black hole produces a jet, the jet will exhibit long-term precession due to the geodetic precession mechanism (Begelman et al. 1980). Jet curvature on large physical scales can therefore, in principle, be used as a mechanism for determining the precession period, and, hence, the angular separation between objects in a binary (see equation 8, reproduced from Krause et al. 2019, hereafter K19). This can be achieved by identifying observable signatures of precession, which appear with different morphological characteristics.

Such observational markers include S-shaped symmetry between the jet and counterjet, curvature of the jet (which can vary from straight to highly curved), multiple or ring-shaped hotspots, and

misalignment between jets and lobes, such as the occurrence of the jet towards the edge of the lobe. A recent analysis of nearby ( $z < 1$ ) radio sources found precession markers in 73 per cent of examined sources (K19). The consequences of jet precession are far-reaching: Active galactic nuclei (AGN) are partly responsible for heating the intracluster medium (ICM, Croton et al. 2006; Best et al. 2007; Turner & Shabala 2015; Raouf et al. 2017), but radio jets may not adequately heat the ICM (Hardcastle & Krause 2013) without an additional mechanism, such as varying jet directions (Babul, Sharma & Reynolds 2013). Accurate predictions of jet morphology may allow for better modelling of AGN feedback effects.

In the coming decades, a new generation of gravitational wave detectors will allow us to detect both transient and continuous sources of gravitational waves (Amaro-Seoane et al. 2012). Even the most massive supermassive black holes will be detectable via the Square Kilometer Array’s pulsar timing array (Wang & Mohanty 2017; Stappers et al. 2018). We can hope to gain first insights into the binary supermassive black hole population from an analysis of the morphology of extragalactic radio sources. Data from surveys such as LOFAR (e.g. Shimwell et al. 2019) have vastly increased the number of known radio-loud AGN sources in the nearby Universe, many of which contain complex morphologies that may exhibit potential precession indicators (e.g. Hardcastle et al. 2019). High-resolution VLA data indicate potential complexities in the jet structure, some of which may be candidates for jet precession (e.g. Mahatma et al. 2019).

\* E-mail: mh17adw@herts.ac.uk

Doppler boosting and relativistic aberration influence the observed jet structure. This becomes more pronounced at higher inclination angles, to the point where the counterjet may be rendered invisible. Conversely, hydrodynamic interactions between the jet, lobe, and ICM can result in light jets being pushed in one direction or another. Here, we will assume that hydrodynamic interactions are negligible, which will be discussed later.

The aim of this paper is to provide an efficient, novel approach to constrain the precession parameters in radio jets that have already been identified as precession candidates. Assuming ballistic precession of a jet emanating in the spin direction from a spinning member of a supermassive binary that undergoes geodetic precession, the precession parameters can be turned into constraints on the binary orbit, thus informing the interpretation of future gravitational wave observations. We will present its efficacy on noisy data, as well as for sources where the knowledge of the jet path is incomplete, and try it on Cygnus A.

## 2 SIMULATIONS

### 2.1 MCMC approach

In this project, we use a Markov chain Monte Carlo (MCMC) approach for jet path determination, based on the PYTHON `emcee` package (Foreman-Mackey et al. 2013). This makes use of the Goodman and Weare affine-invariant ensemble sampler (Goodman & Weare 2010), which is valuable for marginalizing over nuisance parameters from complex models with high-dimensional data, as is the case here.

For nearby ( $z < 1$ ) sources with well-known priors (such as Cygnus A) and a high number of easily identifiable jet knots (typically where the number of observed jet points is higher than the number of model parameters, including nuisance parameters), well-fitting jets can be found by minimizing  $\chi^2$  in a manual or brute-force search of parameter space. However, since the observed sources have complex geometry, and many have not been studied enough to have good constraints on priors, the approach rapidly becomes ineffective in finding the best fits, in the sense that it is hard to demonstrate that a true global minimum has been found, and also computationally infeasible in the case where broad priors require a large parameter space to be searched.

Our model, instead, works on the assumption that the likelihood  $L$  is proportional to the line integral through probability density space:

$$L(p_1, p_2 \dots) \propto \int_M p(\mathbf{x}) d\mathbf{x}, \quad (1)$$

where  $\mathbf{x}$  is a position in two-dimensional space,  $d\mathbf{x}$  is the scalar line element, the integral is evaluated numerically over the jet path  $M$  defined by the model parameters  $p_1, p_2 \dots$  (see the following subsection), and  $p(\mathbf{x})$  is the sum of the probability densities due to all data points at  $\mathbf{x}$ . That is, if there are  $n$  jet knots at positions  $\mathbf{d}_1, \mathbf{d}_2 \dots$  and the error on all positional measurements is taken to be  $\sigma$ , then

$$p(\mathbf{x}) = \frac{1}{n} \sum_{i=1}^n \exp\left(-\frac{|\mathbf{x} - \mathbf{d}_i|^2}{2\sigma^2}\right). \quad (2)$$

In the numerical evaluation of the integral, we break the path up into finitely many points and then iteratively increase the sampling until convergence is reached to a given tolerance level, typically for around 1000 points along the path.

An important detail is the use of a prior inversely proportional to the length of the jet (i.e.  $\int_M d\mathbf{x}$ ). This ensures that the code will not favour arbitrarily long jets that maximize  $L$  by passing close to each data point many times. We also included one extra variance parameter  $V$ , with a half-Cauchy prior, which is added in quadrature to the measurement error on the data points  $\sigma_d$  as discussed by e.g. Hogg, Bovy & Lang (2010): that is,  $\sigma^2 = \sigma_d^2 + V$ . This improves the convergence of the algorithm in the burn-in phase by preventing it from becoming stuck in local minima. This parameter always converges on a very low value by the time burn-in is complete and so we treat it as a nuisance parameter that can be marginalized over in the remainder of this paper.

### 2.2 Precessing jet model

Gower et al. (1982) developed a relativistic jet curvature model for precessing jets where light traveltime is close to jet expansion time (resulting in relativistic aberration effects). They give the instantaneous velocity vector as follows:

$$v_x = s_{\text{jet}} \beta c \left\{ \sin \psi \sin i \cos [\Omega(t_{\text{ej}} - t_{\text{ref}})] + \cos \psi \cos i \right\}, \quad (3)$$

$$v_y = s_{\text{jet}} \beta c \sin \psi \sin [\Omega(t_{\text{ej}} - t_{\text{ref}})], \quad (4)$$

$$v_z = s_{\text{jet}} \beta c \left\{ \cos \psi \sin i - \sin \psi \cos i \cos [\Omega(t_{\text{ej}} - t_{\text{ref}})] \right\}, \quad (5)$$

where  $s_{\text{jet}}$  is a sign parameter corresponding to 1 for the jet, and  $-1$  for the counterjet;  $\beta = v/c$ , where  $v$  is the jet speed;  $i$  corresponds to the inclination angle of the jet along the line of sight;  $\psi$  corresponds to the precession cone opening angle;  $t_{\text{ej}}$  is the ejection time of an individual plasmon (packet of radio energy); and  $t_{\text{ref}}$  is a reference time taken some time after  $t_{\text{ej}}$ .  $\Omega$  is the precession frequency defined as  $\Omega = 2\pi/p$  (where  $p$  is the precession period), and is given in units of radians per second.

From here, the jet path on the sky can be found as

$$\phi_z = v_z(t_1 - t_{\text{ej}}) / [d(1 - v_x/c)], \quad (6)$$

$$\phi_y = v_y(t_1 - t_{\text{ej}}) / [d(1 - v_x/c)], \quad (7)$$

where  $\phi_z$  and  $\phi_y$  correspond to the jet angular motion as viewed by the observer. In the notation of the previous section,  $\mathbf{x} = (\phi_y, \phi_z)$ , up to some unknown position angle  $\alpha$  on the sky. The jet path is obtained by fixing  $t_1$ , the epoch of observation, and varying  $t_{\text{ej}}$  from  $t_1$  to 0, to build up a picture of the jet. The phase angle,  $\theta$ , at the black hole at the time of observation, is given by  $\Omega(t_1 - t_{\text{ref}})$ .

A simulated jet path is shown in Fig. 1. This shows the path for a jet with  $t_1 = 1$  Myr,  $\log_{10}(p/\text{Myr}) = -0.5$ ,  $\beta = 0.6$ , and  $z = 0.1$ .

## 3 RESULTS

### 3.1 Model validation

Model validation was carried out using simulated data. We simulated jets using the model of Section 2.2. We drew data points (positions on the jet, the  $\mathbf{d}_i$  of Section 2) at random from the length of the simulated jets in order to represent the fact that real jets are knotty and not detected continuously along their length. We added independent Gaussian noise in the  $x$  and  $y$  directions on the sky to the  $\mathbf{d}_i$  to mimic the effect of observational uncertainties on the data. Fig. 1 shows the relationship between simulated data and the original samples from the jet and counterjet. In our validation tests, we used a model very similar to that plotted in Fig. 1: in particular,

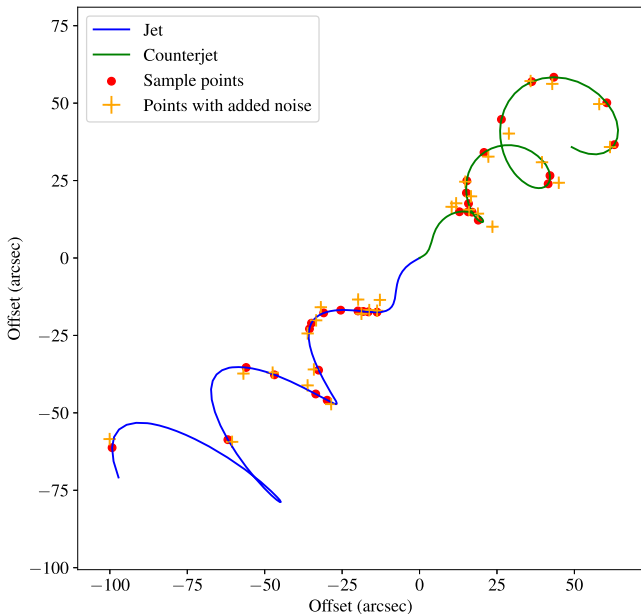


**Figure 1.** Generated data points for a simulated jet and counterjet projected on the sky. This particular example has  $i = 70^\circ$ ,  $\psi = 15^\circ$ ,  $\theta = \pi/2$  rad,  $\log$  precession period of  $-0.5$ , jet speed of  $0.6c$ , and  $\alpha = 135^\circ$  rad. We assume a jet lifetime of 1 Myr and the source is taken to be at  $z = 0.1$ . This example uses 15 data points for each side, resulting in 30 jet points ( $d_i$  from equation 2). Red circles show randomly generated points drawn from the jet/counterjet path shown in blue; orange crosses show the effect of adding independent Gaussian noise to the  $x$  and  $y$  positions, here with  $\sigma = 2.0$  arcsec.

**Table 1.** List of parameters varied during parameter space search. For each combination of parameters, 40 realizations of random point generation and MCMC fitting were produced.

Parameter	Values	Units
Inclination angle	30, 60, 90	Degrees
Precession cone opening angle	15, 30, 45	Degrees
Precession period	$-0.5, 0, 0.5$	$\log_{10}(p/\text{Myr})$

all test simulations had  $\beta = 0.6$ ,  $t_1 = 1$  Myr, and  $z = 0.1$ , as these are reasonable parameters for the type of jet we hope to study. The phase angle  $\theta$  was fixed to  $\pi/2$  rad, as this simply corresponds to a rotation of the precessing jet about its axis and should not affect our ability to recover other jet parameters by fitting.

Initially, we focused on simulated sources where only a single jet is detected. We produced three groups of simulated precessing jets, each with 30 fitted jet points. For each set, we varied one parameter and kept the others constant. Unless otherwise specified, we use an inclination angle of  $70^\circ$ , an opening angle of  $15^\circ$ , and a precession period  $p$  such that  $\log_{10}(p) = -0.5$ , as shown in Fig. 1. The MCMC fitting used 96 walkers and ran for 5000 steps; the first 400 were removed as burn-in. Initial positions of the walkers are drawn uniformly from the priors on each parameter except for jet length (as described in Section 2). We verified by inspection of the tracks taken by the walkers that 400 steps was a conservative value to use for burn-in. This search used flat priors.

For each combination of input model parameters as listed in Table 1, we generated 40 instances of simulated data (as shown in Fig. 1), where each instance generates a different combination of randomly generated points and noise. We ran the MCMC fitting

on each simulated data set, fitting for the inclination angle  $i$ , the cone angle  $\psi$ , the phase  $\theta$ , the precession period  $\log(p)$ , the jet speed  $\beta$ , and the position angle on the sky  $\alpha$ . To characterize the quality of the fits, we took the widths of the distribution functions of the precession period, defined as the distance between the upper and lower bounds of the credible intervals. The credible interval is defined as the 68 per cent confidence interval around the peak of the posterior distribution (the highest posterior density interval). As our figure of merit, we used the credible interval on the posterior probability distribution for precession period, which was invariably peaked close to the true value. For a given set of model parameters, we recorded the means of the widths of the credible intervals on precession period. Standard deviations of the measured widths are roughly 10 per cent of the widths or less. For the inclination angle, we varied the inclination from  $10^\circ$  to  $90^\circ$ . For the precession period, we varied the logarithm of the precession period in Myr from  $-0.5$  to  $0.5$ . Finally, for the cone opening angle, we varied the precession cone opening angle from  $5^\circ$  to  $45^\circ$ . Fig. 2 shows our results. The mean credible interval for our simulated data varies between 0.4 and 0.8, corresponding to uncertainty factors of 1.6–2.5. Smaller credible intervals (i.e. better constrained precession periods) are obtained with inclination angles from  $30^\circ$  to  $80^\circ$ , precession periods in the range 0.5–1 Myr, and opening cone angles greater than  $15^\circ$ .

We conducted a full quantitative search of the parameter space and found it possible to find a peaked posterior distribution for precession period using this method, alongside good constraints on other parameters. We get particularly good constraints (i.e. narrow posterior probability distributions centred round the true values) on position angle  $\alpha$ , phase  $\theta$ , and precession cone opening angle  $\psi$ . The parameter of greatest interest is precession period, as this is the one from which we can obtain information regarding binary separation. We verified that for these simulations we obtain unbiased estimates of the precession period using the median of the posterior probability distribution, as expected.

We investigated how the number of fitted jet points affects fit quality. We therefore repeated the study, but for 20 and 10 simulated points. The result is shown in Fig. 3. We found that 20 jet points performed similarly to 30 points. However, the quality of fits, in terms of the constraints that we obtained on precession period, decreased markedly with 10 points. This is not surprising, given that the number of jet points becomes close to the number of degrees of freedom of the model (6).

### 3.2 Counterjet

All modelling up to here was done with a single jet, the approaching jet: In many real sources, the approaching jet is the only visible one because of the strong effects of Doppler boosting. We also ran models where we distributed the same number of jet points either on the approaching jet, only, or on both, jet and counterjet, in order to find out whether having the same number of points spread over two jets gave a better, worse, or equal fit. Fig. 4 compares a single jet model (red) and one containing both the jet and counterjet (teal; see Fig. 1 for an example of simulated data that include the counterjet.).

For the same set of parameters (here, using one of the better fits identified in the previous parameter study, of  $i = 60^\circ$  and  $\phi = 15^\circ$ ), we observe that the inclusion of a counterjet in an otherwise identical model produces consistently better constrained precession period estimates, by up to 0.3 dex, across 30, 20, and 10 points. Again, fits with 10 data points give only poor constraints on the precession period, but the presence of a counterjet still results in an improvement of 0.1 dex.

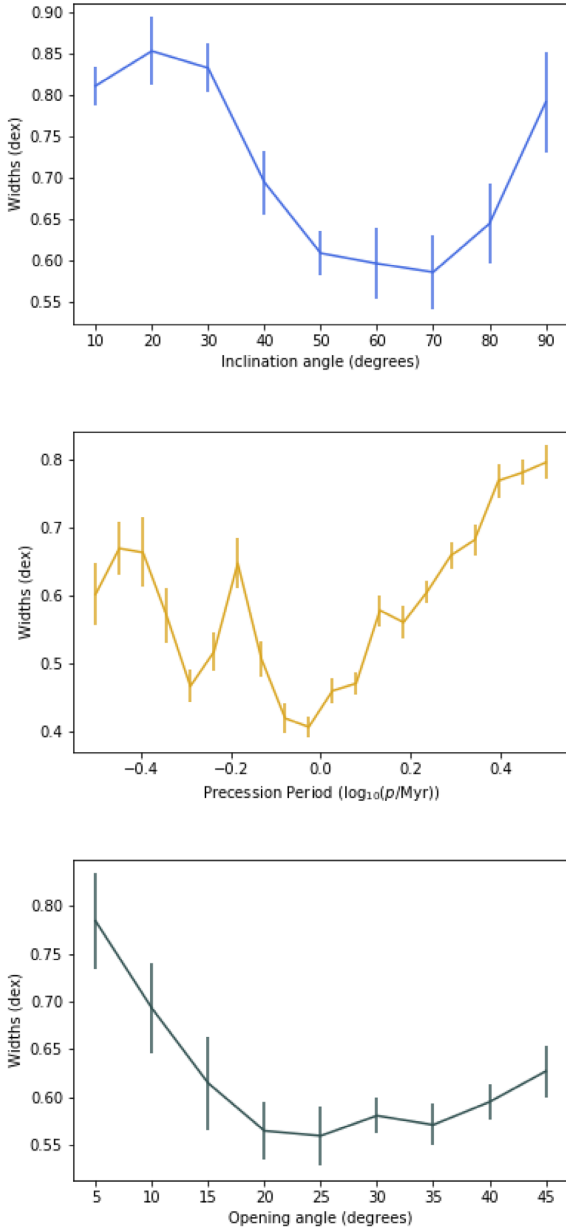


**Figure 2.** Results of parameter study. Each plot shows the mean width of credible intervals for the precession period in dex – i.e. twice the  $1\sigma$  uncertainty in dex – over each parameter that was varied in the specific series of runs. Top panel: Inclination angle varies from  $10^\circ$  to  $90^\circ$ . Middle panel: precession period varies within  $-0.5 < \log(p/\text{Myr}) < 0.5$ . Bottom panel: Precession cone opening angle ranging from  $5^\circ$  to  $45^\circ$ . The constraints on precession period are good (uncertainties less than a factor of 3) across all of the parameter space, with smaller credible intervals being found at higher inclination angles and with a precession period closer to 1 Myr.

Given the relativistic nature of the jet path, we suggest that the improvement when a counterjet is included comes from the additional morphological constraints provided by the receding jet, which is not simply an inverted copy of the jet (as seen in Fig. 1).

#### 4 CYGNUS A

We use the well-studied extragalactic radio source Cygnus A to demonstrate the applicability of our code. This is one of the nearest

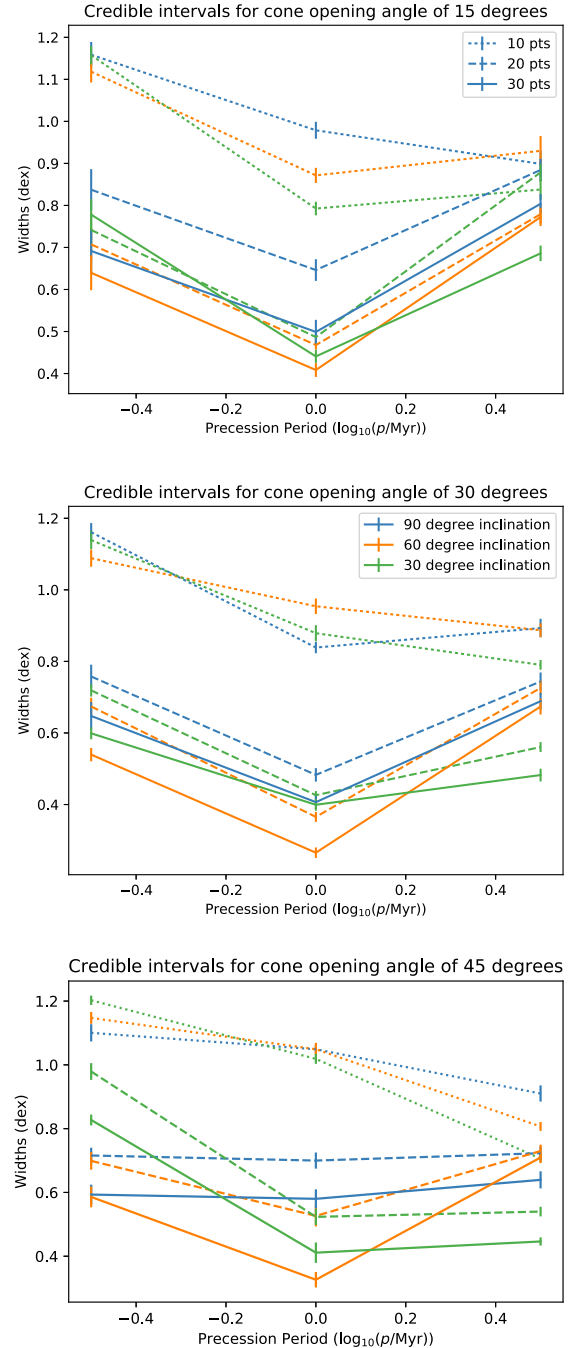


**Figure 3.** Investigation of the number of jet points required to obtain a certain fit quality depending on input parameters. From top to bottom, the precession cone opening angle changes from  $15^\circ$  over  $30^\circ$  to  $45^\circ$ . Blue lines correspond to inclination angles of  $90^\circ$ , orange are at  $60^\circ$ , and green at  $30^\circ$ . Solid lines represent a fit of 30 jet points, dashed lines are 20, and dotted are 10. 20 data points show a marked difference in credible interval widths compared to 10 points, whilst the addition of another 10 has less of an impact.

Fanaroff–Riley type I (FR II) galaxies and has a well-defined jet and counterjet with a jet inclination angle thought to be between  $55^\circ$  and  $85^\circ$  (Bartel et al. 1995), with a redshift of  $z = 0.0562 \pm 0.000067$  (Carilli & Barthel 1996). There is observational morphological evidence to suggest that the jets are precessing (K19).

We visually identified 48 jet points (with an astrometric error of 0.4 arcsec from VLA data) from the 5-GHz map of Perley, Dreher

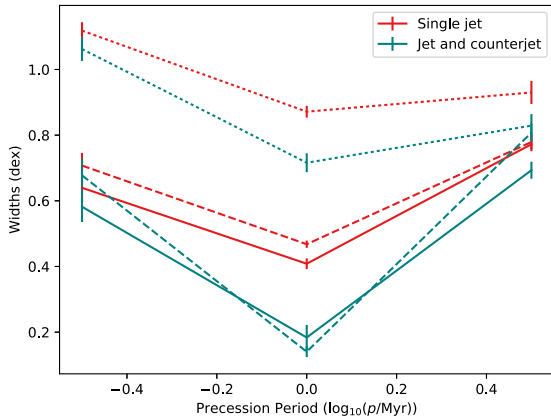


**Figure 4.** Comparison showing credible intervals of a counterjet (teal) and single jet (red) for an inclination angle of  $60^\circ$  and a precession cone angle of  $15^\circ$ . Solid lines represent a fit of 30 jet points, dashed lines are 20, and dotted are 10.

& Cowan (1984), as shown in Fig. 5. Jet points are taken to be any discrete, distinct feature that appears to be part of the jet; this includes both compact knots and sub-regions of more extended bright parts of the jet. For longer sub-regions of the jet, we placed multiple points, spaced by at least the resolution of the image, in order to constrain the curvature of the jet in these regions.

One important constraint on the application of the MCMC model to real-world data is the requirement for the precessing jet to stay within the lobes. Since the model does not take lobe structure into account beyond the terminal hotspot, the constraint was implemented by a joint prior on position angle and precession cone opening angle. This dual parameter calculates the two extreme

edges of the cone for any given position angle, and keeps them within the lobes, which are approximately  $25^\circ$  across at their widest point. Without this additional prior, we found that unphysical jet paths were permitted as part of the fit, broadening the credible interval on precession period. As with the tests described in earlier sections, the priors were flat within the permitted ranges.

We initially fitted the model to all identified points (see Fig. 6), including the terminal hotspot, which in both lobes is taken to be the more compact or ‘primary’ hotspot; we do not include the larger, brighter secondary hotspot since the position of this is almost certainly dominated by post-shock hydrodynamics (Cox, Gull & Scheuer 1991). Then, with respect to the potential for hydrodynamic influences to dominate the jet path within the lobes, we fitted the model only to the straight portion of the jet, terminating just inside the lobes (Fig. 7). The full number of regions produced a peak in the posterior distribution corresponding to a precession period of 1 Myr.

K19 show that, on the assumption that the jet is produced by the more massive black hole, an upper limit on the binary separation in pc,  $d_{\text{pc}}$ , is given by

$$d_{\text{pc}} < 0.18 P_{\text{gp, Myr}}^{2/5} M_9^{3/5}, \quad (8)$$

where  $P_{\text{gp, Myr}}$  is the precession period in Myr and  $M_9$  is the black hole mass in units of  $10^9 M_\odot$ . Our estimated precession period of  $\sim 1$  Myr thus corresponds to an upper limit on the binary separation distance of 0.3 pc. This was calculated using the total central black hole mass of  $(2.5 \pm 0.7) \times 10^9 M_\odot$  (Tadhunter et al. 2003). Using only the straight part of the jet within 50 arcsec from the core results in a preferred range of 1–10 Myr for the precession period with a less probability of up to several 100 Myr.

Since the credible interval on the posterior encompasses a range of precession period values, we can also consider the constraints

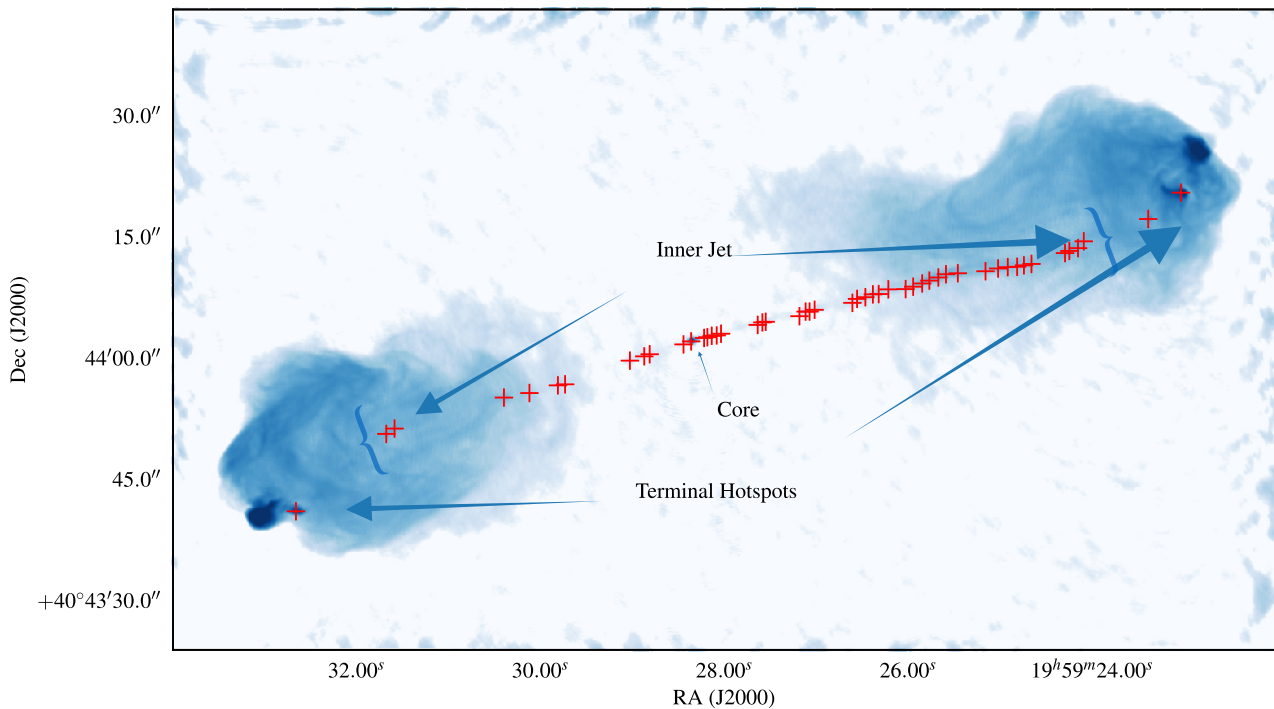


**Figure 5.** Locations of visible jet knots within Cygnus A used in the model. Note the curvature in both the jet and counterjet paths. The final points in both the jet and counterjet lie above the primary hotspots of the two lobes, as discussed in the text. The inner, straighter points of the jet used in Fig. 7 are identified as being within the indicated brackets.

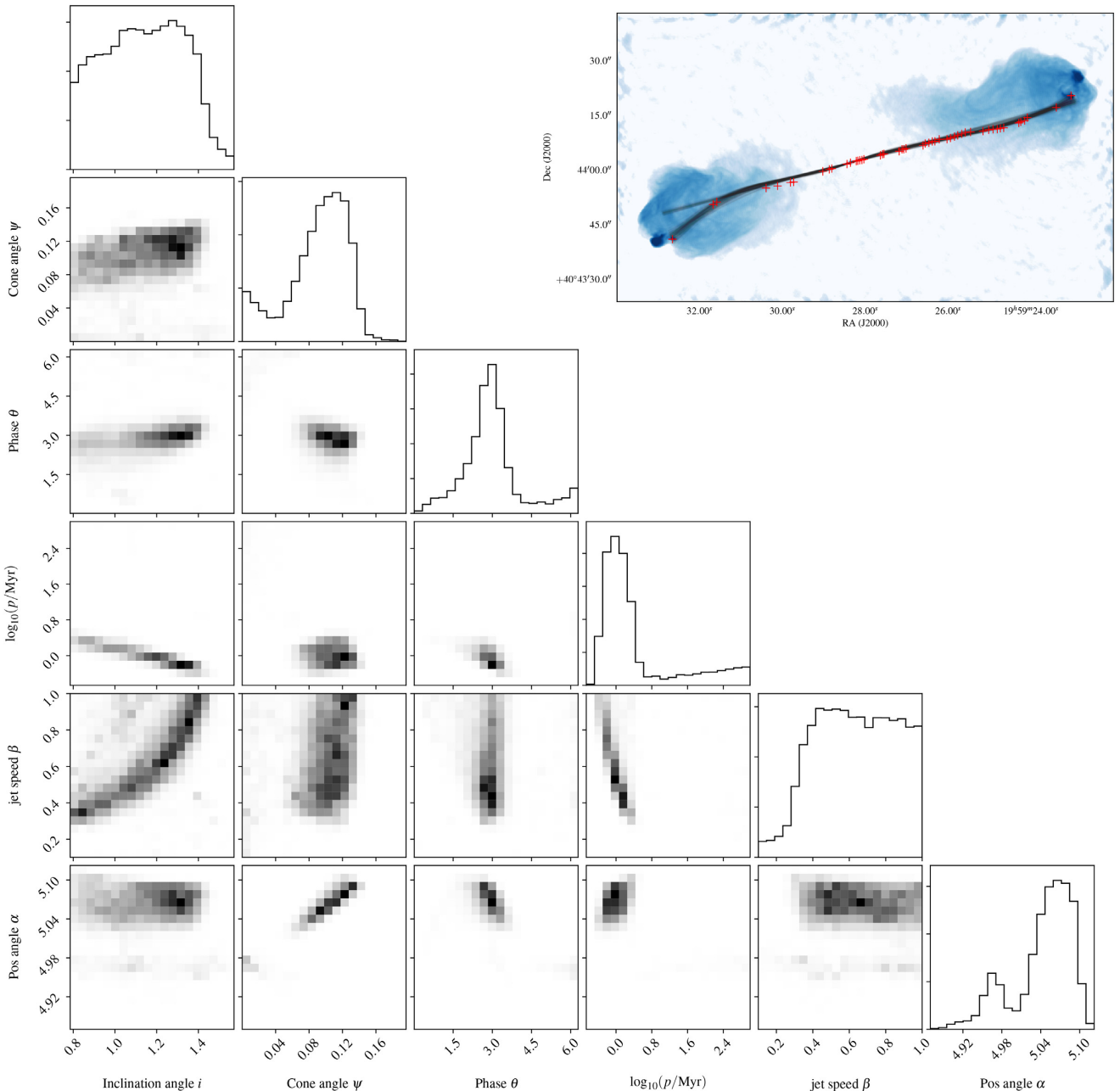


**Figure 6.** Main: ‘Corner plot’ of one-dimensional and two-dimensional marginalized posterior probability distributions for the model parameters, given the observed jet path of Cygnus A, including all identified jet points up to the terminal hotspot. Inset: jet paths based on parameters drawn at random from the posterior overplotted on the radio image of Cygnus A.

given by the full posterior rather than just its peak, as shown in Fig. 8. This shows the cumulative probability distribution in log space of the binary separation limit as calculated from K19. This indicates that the lower limit of the cumulative probability of the separation being  $<0.3$  pc is 0.8, whilst for  $<1$  pc, it is around 0.85, and with least 95 per cent confidence, the separation is  $<2$  pc.

## 5 DISCUSSION

We have shown that strong constraints on precession periods of precessing jets can be obtained with MCMC fitting of the jet path, if the jet is detected at at least 20 points. Even 10 points can yield useful constraints. Furthermore, Fig. 4 highlights that

the presence of a counterjet produces much better fits in an otherwise identical model. That is, a single visible jet with 20 identifiable distinct regions produces less accurate constraints on the posterior distribution than 20 such regions distributed between the jet and counterjet. This is because of the different morphological distortion of the jet and counterjet due to the relativistic aberration, which means that the counterjet is not just a mirror image of the jet.

For 10 data points, we obtain a credible interval width of typically 1 dex, i.e. an uncertainty of a factor of 3 in either direction on the precession period. For 20 data points, this is significantly improved, showing a precision of around 0.4 dex. This is relevant for future binary black hole research. Equation (8) shows that the separation

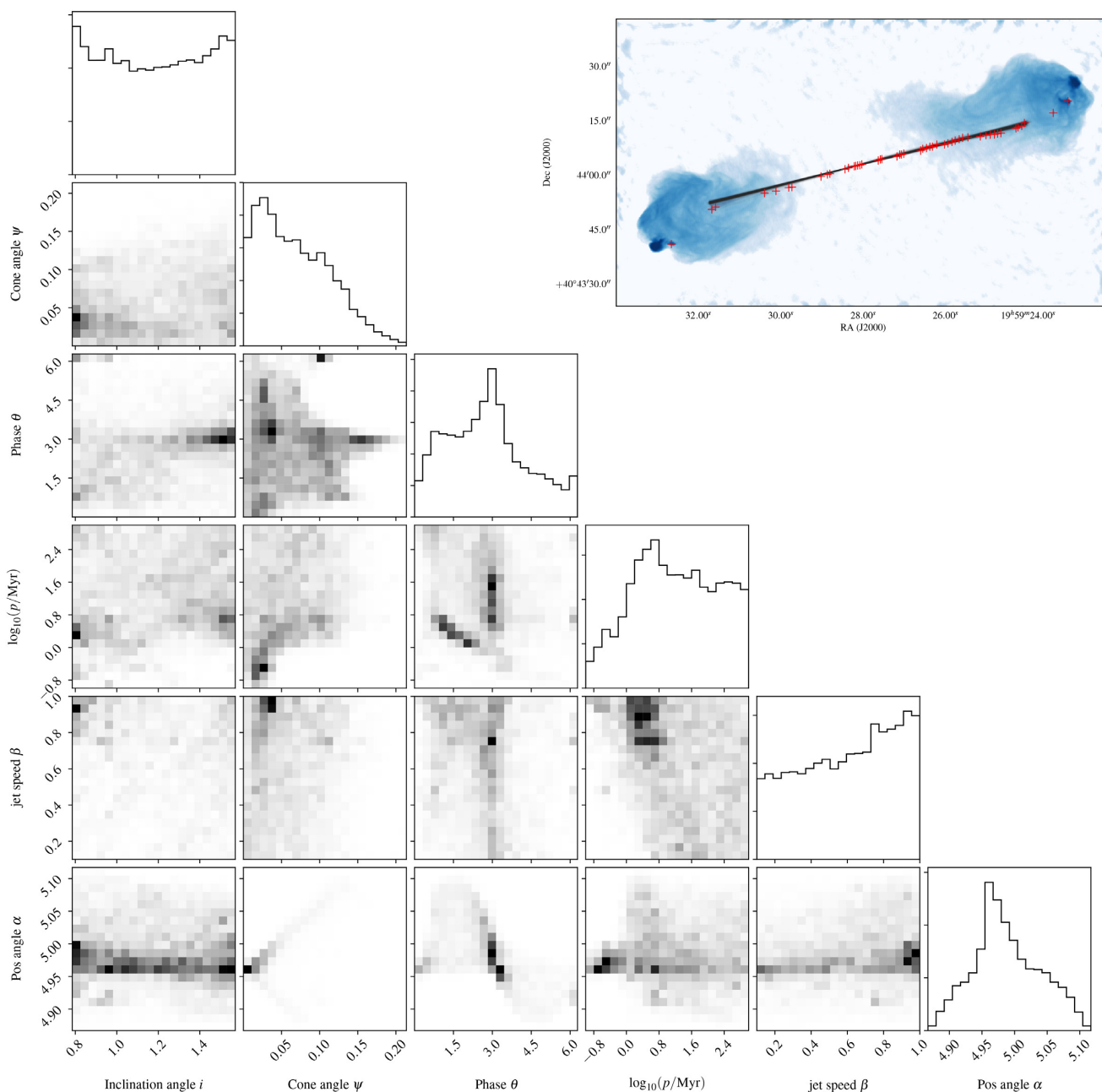


**Figure 7.** Main: ‘Corner plot’ of one-dimensional and two-dimensional marginalized posterior probability distributions for the model parameters, given the observed jet path of Cygnus A, limited to straight portions of the jet. Inset: jet paths based on parameters drawn at random from the posterior overplotted on the radio image of Cygnus A. The jet points used for this fitting are indicated by the extent of the overplotted jet paths.

of a binary black hole can be constrained by the precession period, therefore being able to adequately measure a precession period with uncertainties at the level of 1 Myr means that we can constrain separations to the order of parsecs, assuming that the precession is due to geodetic precession, as discussed in Section 1. This is highlighted by the real-world example of Cygnus A, which shows a probable separation distance of  $<2$  pc, with a peak in the posterior probability corresponding to a separation of  $<0.3$  pc using the equation mentioned above.

The ability to constrain angular separation and detect binary systems from jet curvature, using only 20 jet knots, opens up new possibilities for detecting supermassive black hole binaries using

observational data. We have shown that for jets observed on the arcminute scale, precession periods of around 1 Myr produce better fits even when the inclination angle or cone opening angle does not vary (Fig. 2, all panels). This should not be seen as surprising, since shorter precession periods will produce a more complex jet morphology, and longer periods will result in straighter jets, which are harder to find constraints for.

Cygnus A is an excellent example to discuss possible effects of hydrodynamics. The southwards bend east of  $19^{\text{h}}59^{\text{m}}24^{\text{s}}$  has been suggested to be likely due to hydrodynamics in a comparison of three-dimensional hydrodynamic precessing jet simulations by Cox et al. (1991). Interestingly, the ballistic jet models generally

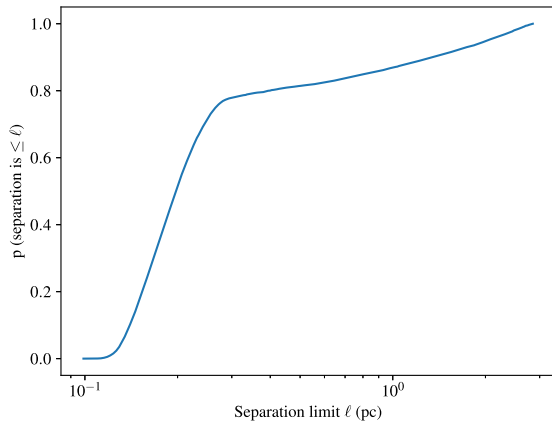


**Figure 8.** Cumulative probability of upper limit on binary separation calculated using equations in K19, using samples from the posterior with burn-in removed.

do not follow this bend (compare Figs 6 and 7). This supports the hydrodynamic interpretation, but does not rule out the possibility that the precession is more complex in nature than the simple conical precession assumed in the models of Section 2.2.

In magnetized jets, current-driven instabilities can dislocate the jet and affect the position of the hotspot (O’Neill, Beckwith & Begelman 2012). Even when the magnetic field is not dynamically important, the vortex shedding at the jet head introduces a complex feedback loop, impacting the jet directly via the ram pressure of the backflow and via locally increased pressure due to shocks in the jet termination region (Lind et al. 1989). Three-dimensional magnetohydrodynamical simulations showed that these dynamics lead to some random dislocation of the jet termination regions (Mignone et al. 2010; English, Hardcastle & Krause 2016), but the effects were found to also depend on the grid resolution in the simulation (Krause & Camenzind 2001).

An important characteristic of the results on Cygnus A is that the fitting is driven by the outer data points located at the primary hotspots; without this, the model cannot constrain precession periods since the resulting jet is too straight to provide constraints on the parameters. Given the impact of the terminal hotspots on the jet model, it is important to understand whether the position of the hotspots is driven more by precession or by hydrodynamics. This will be explored in future work.

We used a broad flat prior on jet speed (varying  $\beta$  from 0.1 to 0.99c), but found that subrelativistic speeds were disfavoured, contrary to the results obtained by Steenbrugge & Blundell (2008). Their model requires the southwards bend in the western jet (which we argued above to be primarily due to hydrodynamic effects) to be explained by the precession model, while they disregard the eastern hotspot for their fit. Jet speeds  $\beta > 0.4$ , as found in our analysis, also agree better with VLBI constraints for Cygnus A (e.g. Boccardi et al. 2016) and general beaming constraints for jets in radio galaxies (Mullin & Hardcastle 2009).

Although in Cygnus A we have well-constrained jet positions, we have found that removing down to  $\sim 30$  data points makes very little difference to precession period constraints, and that constraints can still be found for as few as  $\sim 20$  points, provided that they adequately represent the curvature: As we saw in the case of Cygnus A, removing even a few points in strongly curved regions of the jet can have a negative effect on the precession period constraints. This suggests that the method can be applied to more remote objects with less well constrained jet positions in the future, including sources

with less available data compared to Cygnus A. Given the results of Fig. 2, it is worth noting that some remote galaxies with favourable characteristics may still produce a fit at even less than  $\sim 20$  points, assuming those are distributed over both the jet and counterjet.

Finally, we note that the models of Section 2.2 work on the assumption of a constant jet speed. This rules out their direct application to FR I sources where it is known that the jets decelerate over large scales (Laing & Bridle 2014). The model could, in principle, be applied to such sources if a prescription for jet deceleration were included. Another interesting future improvement might be the inclusion of brightness variations as a consequence of examining the influence of jet speed on apparent surface brightness via Doppler boosting, although this may be challenging in the case of FR II jet sources, which typically show non-uniform surface brightness.

## 6 SUMMARY AND CONCLUSIONS

The key results for this paper are as follows:

- (i) We have developed and tested a MCMC model for fitting the precession period to images of radio galaxy jets.
- (ii) We have shown that it is possible to find good constraints for precession period in simulated data, in suitable conditions, for varying numbers of data points.
- (iii) The appearance of a counterjet helps stabilize the model and produce better constraints on precession period, even using the same number of points.
- (iv) We applied this to real-world data from Cygnus A and identified a range of plausible precession parameters. Interpreting in the framework of binary supermassive black hole systems, and if precession is caused by the geodetic effect, the binary separation was found to be  $< 0.3$  pc.
- (v) One of the biggest influences on the success of the MCMC code comes from the location of the terminal hotspots. Since this is the case, it is crucial to understand the influence of hydrodynamics in the lobes on the path of the jet.

## ACKNOWLEDGEMENTS

We thank the anonymous referee for their very useful report that greatly helped to improve the manuscript. MAH acknowledges a studentship from STFC [ST/R504786/1] and MJH acknowledges support from STFC [ST/R000905/1].

## REFERENCES

- Abbott B. P. et al., 2016a, *Phys. Rev. Lett.*, 116, 061102  
 Abbott B. P. et al., 2016b, *ApJ*, 818, L22  
 Abbott B. P. et al., 2017, *Phys. Rev. Lett.*, 119, 161101  
 Amaro-Seoane P. et al., 2012, *Class. Quantum Gravity*, 29, 124016  
 Babul A., Sharma P., Reynolds C. S., 2013, *ApJ*, 768, 11  
 Bartel N., Sorathia B., Bietenholz M. F., Carilli C. L., Diamond P., 1995, *Proc. Natl. Acad. Sci.*, 92, 11371  
 Begelman M. C., Blandford R. D., Rees M. J., 1980, *Nature*, 287, 307  
 Best P. N., von der Linden A., Kauffmann G., Heckman T. M., Kaiser C. R., 2007, *MNRAS*, 379, 894  
 Boccardi B., Krichbaum T. P., Bach U., Mertens F., Ros E., Alef W., Zensus J. A., 2016, *A&A*, 585, A33  
 Carilli C. L., Barthel P. D., 1996, *A&AR*, 7, 1  
 Carpineti A., Kaviraj S., Hyde A. K., Clements D. L., Schawinski K., Darg D., Lintott C. J., 2015, *A&A*, 577, A119  
 Cox C. I., Gull S. F., Scheuer P. A. G., 1991, *MNRAS*, 252, 558  
 Croton D. J. et al., 2006, *MNRAS*, 365, 11

- English W., Hardcastle M. J., Krause M. G. H., 2016, *MNRAS*, 461, 2025
- Foreman-Mackey D., Hogg D. W., Lang D., Goodman J., 2013, *PASP*, 125, 306
- Goodman J., Weare J., 2010, *Commun. Appli. Math. Comput. Sci.*, 5, 65
- Gower A. C., Gregory P. C., Unruh W. G., Hutchings J. B., 1982, *ApJ*, 262, 478
- Hardcastle M. J., Krause M. G. H., 2013, *MNRAS*, 430, 174
- Hardcastle M. J. et al., 2019, *MNRAS*, 488, 3416
- Hogg D. W., Bovy J., Lang D., 2010, preprint ([arXiv:1008.4686](https://arxiv.org/abs/1008.4686))
- Krause M., Camenzind M., 2001, *A&A*, 380, 789
- Krause M. G. H. et al., 2019, *MNRAS*, 482, 240 (K19)
- Laing R. A., Bridle A. H., 2014, *MNRAS*, 437, 3405
- Lind K. R., Payne D. G., Meier D. L., Blandford R. D., 1989, *BAAS*, 21, 1158
- Mahatma V. H. et al., 2019, *A&A*, 622, A13
- Mayer L., 2017, *J. Phys. Conf. Ser.*, 840, 012025
- Mignone A., Rossi P., Bodo G., Ferrari A., Massaglia S., 2010, *MNRAS*, 402, 7
- Mullin L. M., Hardcastle M. J., 2009, *MNRAS*, 398, 1989
- O’Neill S. M., Beckwith K., Begelman M. C., 2012, *MNRAS*, 422, 1436
- Perley R. A., Dreher J. W., Cowan J. J., 1984, *ApJ*, 285, L35
- Raouf M., Shabala S. S., Croton D. J., Khosroshahi H. G., Bernyk M., 2017, *MNRAS*, 471, 658
- Rodriguez-Gomez V. et al., 2015, *MNRAS*, 449, 49
- Shimwell T. W. et al., 2019, *A&A*, 622, A1
- Stappers B. W., Keane E. F., Kramer M., Possenti A., Stairs I. H., 2018, *Phil. Trans. R. Soc. A*, 376, 20170293
- Steenbrugge K. C., Blundell K. M., 2008, *MNRAS*, 388, 1457
- Tadhunter C., Marconi A., Axon D., Wills K., Robinson T. G., Jackson N., 2003, *MNRAS*, 342, 861
- Tremmel M., Governato F., Volonteri M., Pontzen A., Quinn T. R., 2018, *ApJ*, 857, L22
- Turner R. J., Shabala S. S., 2015, *ApJ*, 806, 59
- Wang Y., Mohanty S. D., 2017, *Phys. Rev. Lett.*, 118, 151104

This paper has been typeset from a  $\text{\TeX}/\text{\LaTeX}$  file prepared by the author.